Energy & Environmental Science

ROYAL SOCIETY OF CHEMISTRY

PAPER

View Article Online
View Journal | View Issue



Cite this: *Energy Environ. Sci.*, 2025, **18**, 9468

# Modeling single-crystal electrodes as a network of primary particles

Pierfrancesco Ombrini, [a] Shakul Pathak,[b] Dimitrios Ntagkras,[a] Santosh K. Pal,[c] Pranav Karanth, [ac] Fokko M. Mulder, [c] Marnix Wagemaker, [a] Martin Z. Bazant [bd] and Alexandros Vasileiadis *[a]

Received 18th July 2025,
Accepted 6th October 2025

DOI: 10.1039/d5ee04131g

rsc.li/ees

Predicting lithium-ion battery behavior is critical for advancing next-generation energy storage. Conventional Doyle–Fuller–Newman models can simulate many materials, but they fail in phase-separating single-crystal systems, such as lithium iron phosphate ($LiFePO_4$, LFP), where the electrical connectivity of primary particles limits charge transport. We redefine the electrode as a network of reactive primary particles, each governed by validated electrochemical kinetics and interconnected through tomographic-informed contact resistances. Without empirical tuning, the model predicts voltage responses of $LiFePO_4$ electrodes across temperatures, rates, loadings, and dynamic load conditions using a single fitted physical parameter. It also captures and explains charge–discharge asymmetries and hysteresis. By bridging particle-scale physics up to cell-level performance, while retaining computational efficiency, this physics-based framework provides a foundation for the design, and control of single-crystal electrode systems.

**Broader context**

Lithium-ion batteries, particularly those based on lithium iron phosphate (LFP), are among the most widely deployed technologies for energy storage, supporting applications ranging from electric vehicles to grid stabilization. Accurate simulations are essential for optimizing performance, extending lifespan, and facilitating integration with renewable energy sources. Yet, while LFP expanded in battery markets, its modelling lagged behind. The conventional Doyle–Fuller–Newman framework, originally tailored to layered oxide spherical agglomerates, can reproduce single-crystal LFP behavior only by relying on extensive empirical fits. This limits predictive power and applicability to new designs or operating conditions. In this work, we introduce a physically consistent and computationally efficient modeling framework that incorporates microstructural information in a network of electrically connected single-crystal particles. Unlike the DFN, this approach enables accurate predictions across a wide range of experimental protocols and temperatures without relying on empirical adjustments and with minimal fitting parameters. By bridging the gap between microstructure and electrochemical behavior, our model not only advances simulation accuracy for single-crystal LFP electrodes but also lays the foundation for modeling future battery chemistries with single-crystal architectures.

## Introduction

Over the past decade, Li-ion batteries have rapidly evolved. Advancements in every scale – from electrode to pack – have significantly boosted the energy and power densities of these batteries,[1] as exemplified by the emergence of lithium iron phosphate (LFP)-based batteries, now dominating the battery market.[2] At the electrode scale, architectures such as graded porosity[3] and multi-layered structures[4] have been exploited for improving long-range ion transport. At the particle scale, electrodes can be manufactured with secondary agglomerated particles or single-crystal primary particles,[5] here termed single-crystal electrodes (SCEs). Secondary agglomerates minimize the internal surface area, thereby reducing electrolyte-induced degradation,[6] but they are prone to fracture;[7] In contrast, SCEs can avoid cracking-induced degradation,[8] thereby improving cycle life and power densities. Active materials with low ionic diffusivity, such as LFP, are typically manufactured as nanometric single crystals, achieving diffusion times on the scale of milliseconds[9] and resulting in a reaction-limited process.[10,11]

Yet commercial SCEs fall short of these rate capabilities, indicating the presence of additional limiting factors. Ionic transport

[a] *Department of Radiation Science and Technology, Delft University of Technology, Delft, 2629JB, The Netherlands. E-mail: a.vasileiadis@tudelft.nl*
[b] *Department of Chemical Engineering, Massachusetts Institute of Technology, Cambridge, MA 02139, USA*
[c] *Department of Chemical Engineering, Delft University of Technology, Delft, 2629JB, The Netherlands*
[d] *Department of Mathematics, Massachusetts Institute of Technology, Cambridge, MA 02139, USA*

in the electrolyte can limit high-loading electrodes (>3 mAh $cm^{-2}$),[12] but thin high-power electrodes mitigate this issue. For the latter case, the performance of SCEs composed of insulating materials are impacted by the inter-particle electrical connectivity.[13] This is evident by their ability to reach 9-seconds discharge when very high (63%) carbon loading is used[14] and by the significant improvements of LFP performances when carbon coating is applied.[15] The work of Li *et al.*[13] shows that the reaction initiates from particles connected to the carbon black (CB) and propagates then towards the unconnected ones, demonstrating that inter-particle electron transport, coupled with local reactions with the electrolyte, is at the core of the reaction mechanism. Additional evidence is provided by the significant performance losses of LFP electrodes in cold conditions,[16] compared to layered oxide electrodes. The reason lies in the electrical conductivity of the carbon coating decreasing sharply at low temperatures,[17] since the electrons hopping between metallic $sp^2$ and insulating $sp^3$ domains introduce a macroscopic energy barrier.[17]

Considering the growing importance of SCEs, especially those based on LFP, it is necessary to develop reliable numerical models to operate them in control-oriented tasks.[18] While data-driven approaches can be employed,[19] they cannot extrapolate beyond the data and provide little physical insight. Physics-based modeling, in contrast, can predict battery performances under new condition and accelerate electrode development[20] by optimizing CB content, thickness, and porosity.[21] However, despite advances in the characterization of SCEs,[5,13] these systems have not been comprehensively modelled.

Doyle–Fuller–Newman models (DFN)[12,22] can achieve precise results with limited computational cost,[23] making them attractive for practical applications. Ionic transport in the electrolyte is captured by adjusting diffusivity and conductivity base on porosity and tortuosity.[12,22] Similarly, electron transport through the solid phase is modelled using Ohm's law.[24] The electrode is divided into discretized volumes, containing a set of independent particles and having uniform electrolyte and electrical potential. The local reaction rate depends on the specified reaction kinetics and solid-state diffusivities. DFN models perform reasonably well when applied to single-phase diffusion-limited materials such as transition metal oxide, especially if concentration-dependent diffusivities and reactivities are considered.[3]

Thomas-Alyea[25] and Safari,[26] expanded DFN models by considering the limited electrical conductivity of LFP and the role of CB-connectivity, enabling them to capture both constant current and path-dependent voltage profiles of an LFP electrode. However, empirical relations were necessary to fit the data, and phase-separation kinetics was entirely neglected. Materials such as $LiFePO_4$,[27] $LiMn_yFe_{1-y}PO_4$,[28] $Li_4Ti_5O_{12}$,[29] and graphite[30] have instead a thermodynamic driving force to separate into Li-rich and Li-poor phases. Capturing this mechanism is essential to capture the electrode-scale behaviour. For this scope, multiphase porous electrode theory (MPET)[31] has been developed by combining DFN and phase-field models, *i.e.*, computing the chemical potential starting from the free energy functional and accounting for the energy penalty of phase boundaries.[24] Using this method, one can model charge–discharge asymmetries in reaction kinetics,[32] voltage hysteresis,[33] active particle population dynamics,[34] and Li-plating on graphite.[30] However, key morphological descriptions are necessary, as exemplified by the case of graphite electrodes, where hierarchical structures[30] were considered necessary to achieve an accurate fit of MPET simulations to experimental data. Similarly, for LFP, the electrical connectivity of primary particles must be considered, as it plays a critical role in shaping the electrode's behaviour.

In response to these challenges, this study proposes a new paradigm for modeling SCEs: instead of treating the electrode as a collection of particles governed by Fickian diffusion, it is modelled as a network of electrically connected nanoparticles governed by Kirchhoff's law. Reconstructing a commercial electrode with focused ion beam scanning electron microscopy (FIB-SEM),[35] followed by segmentation and particle identification, we abstracted the three-dimensional microstructures into a network. The model incorporates inter-particle connectivity,[36] which governs the local voltage drop and, consequently, the single-particle reaction rate. Furthermore, individual particles are modelled using validated approaches,[24] including coupled ion-electron transfer kinetics (CIET)[37] and phase-field modelling,[38] all integrated into a consistent modeling framework.

This fast and scalable approach is here applied to LFP, due to its growing importance in the battery market.[39] However, it is adaptable to a broad range of single-crystal, reaction-limited electrochemical systems. The resulting model bridges diverse electrochemical protocols, including imposed current (CC) and galvanostatic intermittent titration technique (GITT), across varying temperatures, using only one fitting parameter, thereby delivering both accuracy and versatility. Finally, by being firmly rooted in physics and devoid of empirical equations, the model effectively captures the internal mechanisms of SCEs, making it a valuable tool for advancing electrochemical modeling.

### The electrode as a network of connected reactive particles

Tomographic information of a commercial LFP electrode was obtained using FIB-SEM (Fig. 1a). After segmentation,[43] the stack was divided in cubic sub-volumes, and the individual particles were identified (Fig. 1b). Each sub-volume was abstracted as network, by processing the particle–particle and the particle-CB contact areas in adjacency matrices where each pixel records the contact area between two particles or between the particle and the CB phase (Fig. 1c). Using these matrices we constructed a set of graphs[42] where each node stores the information on the particle's size and active surface area. Each edge represents relative contact areas, with CB treated as a source node (Fig. 1d). The segmentation details and their statistics are provided in the SI Methods, alongside the description of algorithms used for the construction of the networks (Fig. S8).

The resulting networks can simulate the reaction kinetics of the microstructure by enforcing current conservation at each

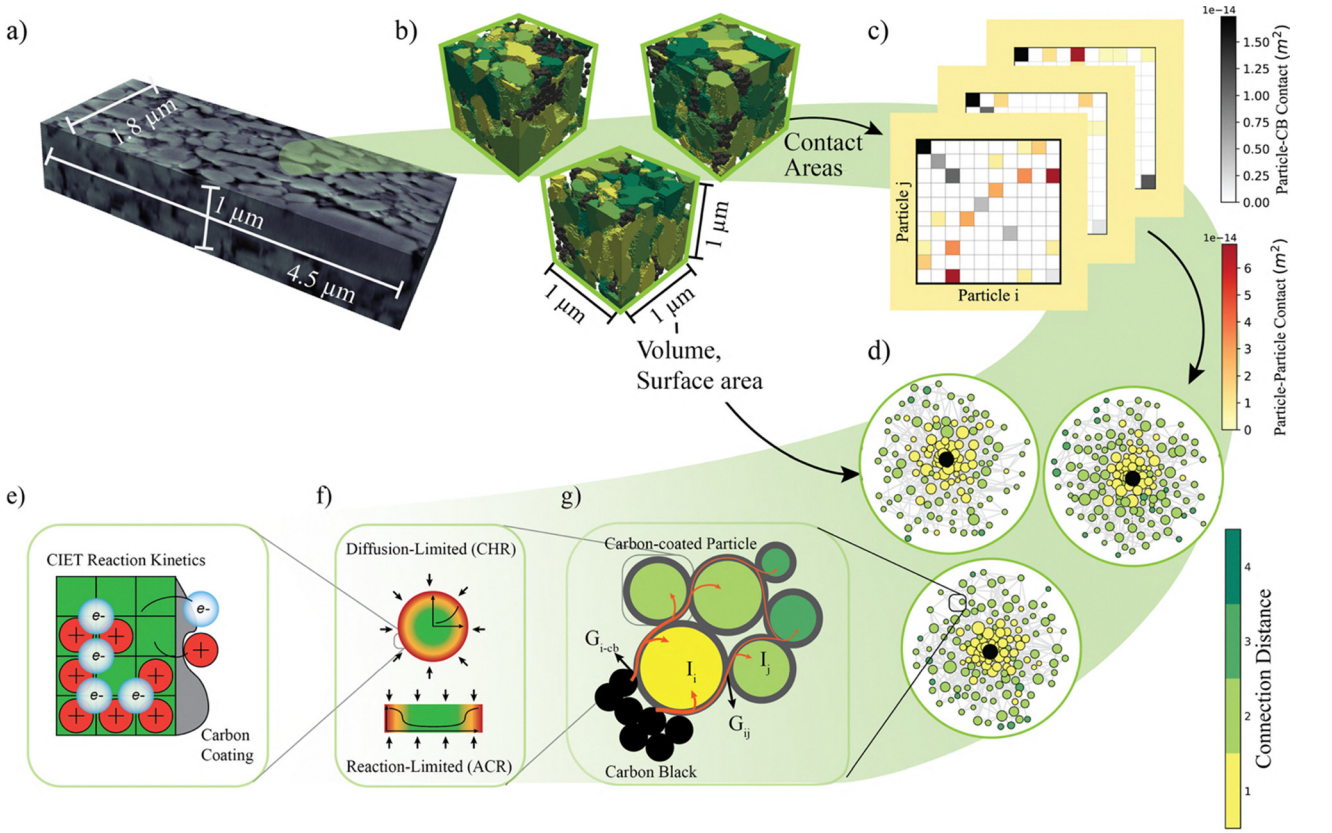


Fig. 1 Multiscale model of single-crystal electrodes. (a) Volume reconstructed from FIB-SEM scans. (b) Segmented sub-volumes. Black particles correspond to the reconstructed[40] spherical nanoparticles of the CB particle phase, the green scale particles correspond to labelled LFP particles, and the transparent regions correspond to the porosity. The segmentation procedure is presented in the Fig. S1–S7. (c) Example of adjacency matrix. The copper scale refers to the inter-particle contact, and the greyscale on the diagonal to the particle-CB contact. The details on its construction are presented in Fig. S8. (d) Network graphs obtained from the segmented sub-volumes, with node size proportional to the particle volume and the colour scale representing the connection distance from the CB node. The graph layouts were plotted using the ForceAtlas2 algorithm[41] of NetworkX,[42] weighted by contact area. The details are presented in Fig. S8. (e) Schematic of the coupled ion-electron transfer model used to simulate the reaction kinetics. (f) Schematic representation of two limiting models that can be used to simulate single-particle reaction kinetics. (Top) Diffusion-limited behaviour modelled by the Cahn–Hilliard Reaction (CHR), showing concentration gradients within the particle and uniform reaction along the surface. (Bottom) Reaction-limited behaviour described by the Allen–Cahn Reaction (ACR), showing concentration gradients along the surface and uniform concentration within the particle. (g) Schematic representation of the network conductance paths. The particle $i$ with connection distance 1 (yellow) is connected to the carbon black through a conductance $G_{i-cb}$ and to the particle $j$ with connection distance 2 (light green) through a conductance $G_{ij}$. The particles react with the electron and electrolyte reservoir with currents $I_i$ and $I_j$, respectively. The electric current (orange lines), originating from the carbon black, is consumed by the particles as expressed in the Kirchhoff's law.

node (Fig. 1g). Assuming that the primary electrical potential losses occur at contact interfaces and that the particle's surface is equipotential, the inter-particle and CB contact conductance ($G_{ij}$ and $G_{i-cb}$) are taken proportional to the contact areas.[44,45] Considering the inter-particle contact areas remain constant during cycling, the constitutive law of the discretized sub-volume can be expressed for each particle $i$ as:

$$I_i\left(\varphi_i, \mu_{\mathrm{surf}_i}, \mu_{\mathrm{elyte}}\right) - G_{i-\mathrm{cb}}\left(\varphi_i - \varphi_{\mathrm{cb}}\right) - \sum_{i \neq j} G_{ij}\left(\varphi_i - \varphi_j\right) = 0$$

where the $I_i$ is the current consumed by the reaction, the second term is the current delivered by the CB, and the summation accounts for the current exchanged with adjacent particles. In this framework, the electrical potential driving a particle's reaction ($\varphi_i$) reflects the influence of the surrounding particle network and the CB potential ($\varphi_{cb}$). The electrical and ionic potentials ($\varphi_{cb}$ and $\mu_{elyte}$) depend on electron and ion transport along the electrode thickness, where percolation is assumed, integrating information about the depth of the simulated sub-volume and the electrode's porosity and tortuosity.[46] These assumptions might not hold true if the carbon coating is not uniform along the particles' surface; however, this is rarely the case in commercial samples.

This framework can be combined with validated single particle models to compute their surface chemical potentials ($\mu_{surf_i}$): 0D homogeneous particles;[33] 1D diffusion-limited particles[29] (Cahn-Hillard approach[29]) or 1D reaction-limited particles[28,38] (Allen-Chan formalism[38]) (Fig. 1f). This follows established multiphase porous electrode theory models.[31] Considering chemo-mechanical effects, which tend to suppress phase separation within submicron-sized particles,[38,47–49] we adopted the 0D approximation (Fig. S11), which reduces

 

the computational cost, while still capturing inter-particle phase separation[33] (Fig. S12). Furthermore, we describe the reaction kinetics $I_i$ using models validated by direct imaging of lithium intercalation dynamics in both LFP single-crystal particles[32] and LFP porous electrodes,[34] *i.e.*, using the electron-transfer-limited version of CIET[37,48] (Fig. 1e). The complete mathematical formulation appears in SI Methods.

The obtained networks reveal the electrode's microstructural properties (Fig. 2). Computing the shortest path from each particle to the CB node defines its connection distance, *i.e.*, the minimal number of edges separating it from CB. Most particles lie one or two edges away (*i.e.*, having a connection distance of 1 or 2), while a few require three or four (Fig. 1d and 2a). Particle size distribution plays a significant role in shaping these statistics. Larger particles are more likely to directly contact the CB phase (Fig. 2b) and exhibit more inter-particle contacts (Fig. 2c). Therefore, they enhance the network's connectivity and ensure uniform current distribution. Hence, despite relying solely on small particles, which might appear advantageous for faster particle-level kinetics, they increase the connection distance, thereby diminishing the electrode's rate capability. While a more uniform CB distribution might mitigate this, achieving it in practice is challenging and risks disrupting the percolation network, which is essential for electronic conductivity. This analysis, further detailed in the Fig. S9 and S10, helps justify the choice of using a bimodal particle size distribution, where smaller particles can fill the larger voids of the larger particles and explores the connectivity statistics of the SCEs, which must be considered in careful electrode engineering.

### Intercalation dynamics in single-crystal electrodes

To verify the model's accuracy in predicting the electrochemical response of real porous electrodes, we compared it with a set of experimental measurements conducted on the sample characterized in this work. All parameterization details, including porosity and tortuosity implementation based on microstructural characterization, are provided in the SI (Fig. S13–S15 and Tables S1–S3).

As a result of the precise characterization, the model requires only one fitted parameter: the inter-particle conductivity $\sigma$. This parameter, determining the utilizable capacity (Fig. S16), is highly sensitive to the synthesis path and carbon coating quality. The reduction to a single fitted parameter enhances model identifiability, allowing for precise estimation that only requires one cycle as a dataset. Finding $\sigma$ by solely fitting the 2C discharge cycle of the 1 mAh cm$^{-2}$ sample, the model replicates constant current (CC) charge and discharge across multiple C-rates (Fig. 3a), including the ones of a higher-loading sample (2 mAh cm$^{-2}$, Fig. S17). This also further confirms the kinetically limiting factor lies in the local particle wiring.

Beyond reproducing voltage responses, the model allows for a detailed investigation of the internal dynamics. In agreement with experiments[13] the system initiate with full (de)lithiation of the particles directly connected with the CB and gradually expands deeper into the network (Fig. 3c). By defining as active particles those within the spinodal range (0.15–0.85 filling fraction), we observed the active particle population evolving in distinct waves (Fig. 3d): first the particles having a connection distance of one or two, only after most of these particles complete their reaction, the poorly connected particles are activated. High-potential electrons from the CB are consumed by the (de)lithiation of the nearest particles, preventing the particles deeper in the network from participating. In other words, the reaction evolves within the local networks, while not being limited by the long range electronic or ionic transport (Fig. S18 and S19). This is also validated by the similar capacities achieved by both the 1 mAh cm$^{-2}$ and the 2 mAh cm$^{-2}$ samples (Fig. S17).

By integrating the network framework with CIET[32,48] reaction kinetics, the model captures charge–discharge asymmetry at the electrode level (Fig. 3a) and explains its origin through the lens of electro-autocatalysis.[34,50] The asymmetry arises from the concentration dependence of the exchange current density, $i_0(c)$[37] (Fig. 3e). During delithiation (charging), lithium removal increases $i_0(c)$, accelerating ion extraction—an autocatalytic effect. During lithiation (discharging), lithium insertion decreases $i_0(c)$, slowing the

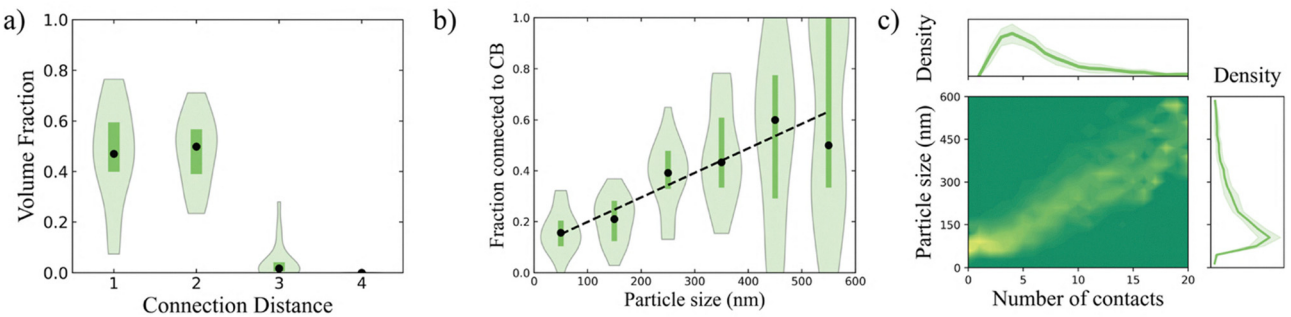


Fig. 2 (a) Distribution of volume fraction as a function of connection distance. The width of the violin represents the density of the specific volume fraction across the sub-volumes. (b) Fraction of directly connected particles as a function of particle size with 100 nm bin size. The width of the violin represents the probability density for the given size range (100 nm). (c) The contour plot shows the relation between particle size and number of contacts. The line plots illustrate the probability density for the number of contacts and particle size distributions across various sub-volumes. The shaded areas (or error bars) represent confidence intervals of ±1 standard deviation.

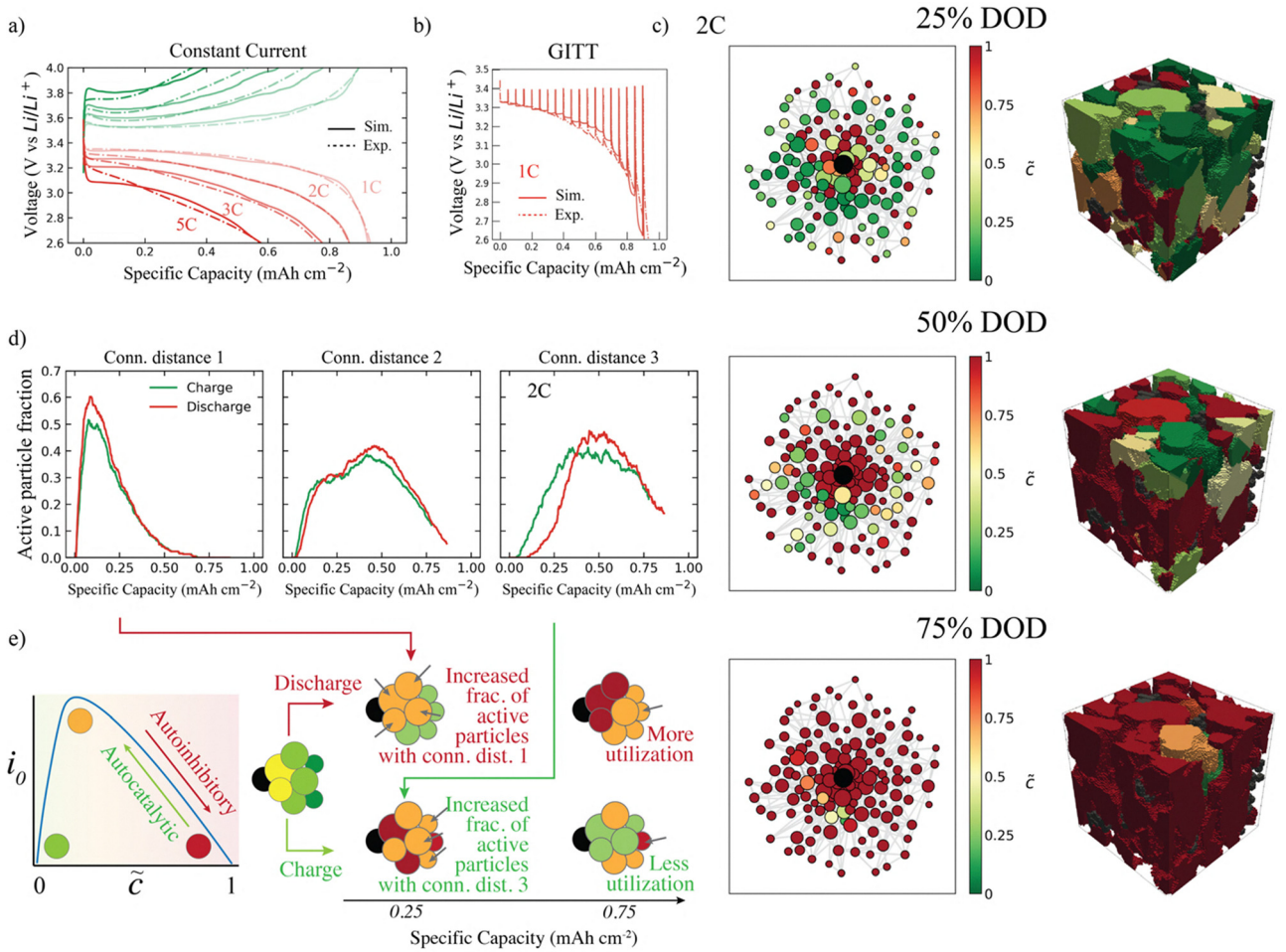


Fig. 3 Dynamics of lithium intercalation in a single-crystal electrode. (a) Comparison between the experimental and simulated voltage curves for 1C, 2C, 3C, and 5C for discharge (red) and charge (green). (1C = 1 mA cm$^{-2}$). (b) Comparison between the experimental and simulated voltages for the GITT protocol. Each pulse delivered 1C current and lasted 3 minutes. The resting time is 30 minutes. (c) Evolution of the particle network and its corresponding microstructure during 2C discharge at different depths of discharge (DOD). The color scale shows the degree of lithiation of the particles. (d) Evolution of the active particle population during a 2C discharge (red) and charge (green), divided by connection distance. Each percentage is calculated based on the population having the corresponding connection distance. (e) Schematic representation of the autocatalytic/autoinhibitory reaction kinetics and its effects on the active particle population dynamics.

reaction—an autoinhibitory effect. During charging, the autocatalytic feedback accelerates the delithiation of particles directly connected to the CB. Fewer particles are thus needed to sustain the current (Fig. 3d) and are depleted, they become inactive early in the charge process. Consequently, the system is forced to rely on more distant particles (*e.g.*, connection distance three) earlier than it otherwise would. These deeper particles are then less available in later stages, requiring higher overpotentials, and thus limiting overall charge capacity (Fig. 3d). In contrast, during discharge, the autoinhibitory effect slows the lithiation reaction, and the reduced local current demand allows electrons to bypass front-line particles and reach deeper ones with limited potential losses, enabling greater capacity. These predictive insights emerge only through the combined use of quantum-informed reaction kinetics and the network-based transport formalism. As such, the model offers a physically grounded explanation for charge–discharge asymmetry and provides a foundation for optimizing operational protocols.

Our model also clarifies the poor correlation between particle size and degree of lithiation. Both nucleation theory[47] and the increased surface-area-to-volume ratio should improve the rate capabilities of smaller particles. Despite this, both experimental observation[51] and our model show little correlation between particle size and filling fraction (Fig. S20). The higher average connectivity of bigger particles offset their kinetics and thermodynamic disadvantages, leading to a more equilibrated lithiation profile.

The uncovered mechanism is also key to understanding the response observed under the GITT protocol (Fig. 3b). Despite 30-minute rest periods, a steadily increasing potential drop is observed after each pulse. Our model explains this behaviour by capturing the interplay between phase separation and electronic connectivity. Initially, the particles are in equilibrium in the delithiated state. During the first pulses, the lithiating particles are those having stronger connectivity to the CB, allowing for low overpotentials. During rest, the phase separation prevents

 

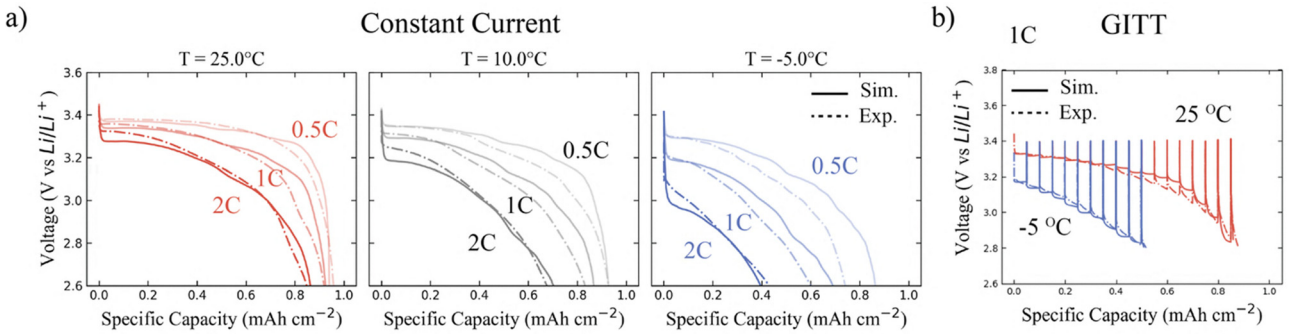


Fig. 4 Effect of temperature on the kinetics of single crystal electrodes. (a) Comparison between the experimental and simulated voltage curves for 0.5C, 1C and 2C discharges at 25 °C, 10 °C and −5 °C. (b) Comparison between the experimental and simulated voltage curves for the GITT protocol. Each pulse delivered1C current and lasted 3 minutes. The resting time is 30 minutes.

equilibration, inducing instead a mosaic arrangement of Li-rich and Li-poor particles. In subsequent pulses, the reaction front progresses deeper into the network, and activating poorly connected particles requires increasingly higher overpotentials. The same model properties are responsible for capturing the thermodynamic hysteresis between charge and discharge, without specialized algorithms[53] (Fig. S21), and the kinetically induced memory effect[52] (Fig. S22 and S23).

Finally, the advantage of our network formalism becomes particularly clear when compared to a conventional DFN model.[54] This model can be tuned by adjusting diffusivity and bulk electrical conductivity to match capacity retention under constant-current conditions (Fig. S24). However, significant changes in bulk conductivity are required to account for the performance difference between the 1 mAh $cm^{-2}$ and 2 mAh $cm^{-2}$ electrodes. Due to the missing physical consistency, the DFN model lacks predictive transferability for guiding electrode design. Assuming Fickian diffusion and neglecting phase separation, this approach also prevents it from capturing the system's response under GITT protocols (Fig. S25); a critical feature for battery control under dynamic operating conditions.[55] Other models, comprehending phase separation but neglecting wiring effects, also fail in capturing the voltage profiles (Fig. S26 and S27). In contrast, our network model naturally captures these phenomena, enabling mechanism-based predictions. This highlights the need for physically grounded approaches that go beyond blind parameter fitting and provide robust insights into performance-limiting mechanisms.

## The effect of temperature

Temperature-dependent tests provide a final validation for our model. This is obtained by including an Arrhenius-like temperature dependence of the electrical conductivity ($\sigma(T) \sim e^{-E_\sigma/k_B T}$), originating from the conduction mechanism of the amorphous carbon coating.[17] Adjusting the previously measured activation energy[17] to 0.32 eV, by fitting the 2C discharge at 10 °C, the model closely matches the experimental data for multiple C-rates at 10 °C and extrapolates the −5 °C behaviour (Fig. 4a). Moreover, the difference between the GITT response at 25 °C and −5 °C is also captured, further supporting the model's validity (Fig. 4b). Although electrolyte conductivity already varies with temperature,[56] we show in Fig. S28 how accounting for $\sigma(T)$ is necessary to reproduce the low-temperature data. Moreover, we show the active particle population is not significantly affected by the temperature change (Fig. S29). Two counteracting factors – the increase in charge transfer resistance and the decrease of electrical conductivity – play opposite roles. Finally, the obtained activation energy is distant from that of the LFP bulk conductivity ($\sim$0.5 eV)[57] further proving the contact resistance to be the limiting factor. While electrolyte engineering is still important, these findings direct the attention to enhancing carbon coatings or introducing carbon nanotubes to improve low-temperature performance of SCEs.[58]

## Conclusions

Modeling of Li-ion batteries can play a crucial role in optimizing their performance and lifespan.[2] Despite its importance, existing porous electrode theories have deficiencies that render them unreliable for SCE. Unifying microstructural imaging, network science, and first-principles kinetics, we present a framework that integrates the microstructural information into a reduced-order formalism. After abstracting the microstructure into a network of electrically interconnected particles, we found that the relationship between the particle size distribution and the CB volume fraction can shape the network's properties.

Moreover, validated models describing single-particle behaviour are integrated with the network framework, creating a robust, physics-based simulation. By grounding the model on the system's physics, the unknown parameters can be accurately found using a limited dataset, enabling reliable predictions. The resulting model demonstrates exceptional generalization across various experimental conditions, including varying protocols, temperatures, and electrode loadings. The critical role of integrating both network abstraction and phase separation into the model becomes particularly evident in intermittent current scenarios,

such as GITT, where conventional DFN models fail to predict the electrode's dynamics. By accounting for phase separation, the model preserves inter-particle heterogeneity during open-circuit conditions, while the network ensures that the multi-particle lithiation sequence is faithfully respected. This physics-informed approach allows the model to accurately predict voltage responses based on both state of charge (SOC) and prior cycling history. Combined with its limited computational cost ($\sim$0.5 minutes for a constant current simulation), these capabilities make the model highly effective in predicting voltage responses under real-world, dynamic input conditions.

Better accuracy and predictivity are coupled with a deeper fundamental understanding. Beyond long-range electron transport, the CB spatial distribution has a drastic influence on the local dynamics (Fig. S30 and S31) and the low-temperature performance of LFP electrodes (Fig. 4). This framework, when coupled with microstructure generation,[40,59] can also predict and optimize the effects of porosity, particle size, and CB volume fractions. For example, an increase in porosity, if leading to a decrease in inter-particle connectivity, might result in unexpected performance losses. Additionally, this framework can be expanded in future studies. For instance, the concept of a particle network could be used to investigate degradation mechanisms by including dynamic detachment[36] of particles during cycling. Moreover, other chemistries, such as Ni-rich or Na-based cathodes, could be modelled in the same fashion as they can show signs of electrical wiring limitations.[44,60,61]

In conclusion, this modeling approach holds broad application potential, spanning solid-state batteries, emerging chemistries, and, more generally, reaction-limited electrochemical systems. Through this study, we have laid a strong foundation for the development of more efficient and reliable energy storage solutions, addressing the increasing demands of modern technology and advancing sustainable energy applications.

# Methods

### Coin cell preparation and cell cycling

The single-crystal $LiFePO_4$ coated electrodes were acquired from CustomCells® in two loadings: 1 mAh cm$^{-2}$ and 2 mAh cm$^{-2}$. The electrodes were cut into disks of 12.7 mm diameter and dried under vacuum at 80 °C overnight prior to cell assembly. The coin cells were assembled in an Argon glovebox using the LFP electrodes, a 25 μm thick Celgard 2500® separator, and a 250 μm thick, 15.4 mm diameter Li metal counter electrode. 1 M lithium hexafluorophosphate ($LiPF_6$) in ethylene carbonate (EC):dimethyl carbonate (DMC) (1 : 1 vol%) was used as the electrolyte. The assembled coin cells were cycled using a LANHE® battery tester inside a climate-controlled climate chamber. Prior to testing, the cells underwent two formation charge–discharge cycles at 0.1C, where 1C corresponds to either 1 mA cm$^{-2}$ or 2 mA cm$^{-2}$, depending on the electrode. The rate performance was evaluated as follows: the cells were charged and discharged at the target C-rate until reaching the cutoff voltage (4.0 V for charge and 2.6 V for discharge), followed by a 1-hour rest period. Subsequently, the cells were charged and discharged at 0.5C until the cutoff voltage was reached, and then they were held at this voltage until the current decreased to C/20. This second step ensured that the electrodes reached fully (de)lithiated states, facilitating parameterization of the simulations. The same protocol was applied at all tested temperatures. The GITT protocol also followed the same procedure, with 20 pulses at 1C (1 mAh cm$^{-2}$) lasting 3 minutes, followed by a 30-minute rest.

### Electrode characterization

The electrode's weights and thicknesses were measured by scraping a region of the electrode, flattening the remaining Al, and measuring their weights and thicknesses. The values were subtracted from the weight and thickness of the coated sample. The thickness was found to vary from 28 μm to 31 μm across the samples, and the weight was found to vary accordingly. The stated electrodes' composition by weight is 90% LFP, 5% carbon black, and 5% binder. These electrodes have a net weight of 9.2 mg and a thickness of 30 μm, leading to the estimation of the volume fractions: 27% porosity, 60% active material, 6.3% carbon black, and 6.7% binder. The 1 mAh cm$^{-2}$ LFP electrode was used to acquire the scanning electron microscopy (SEM) and the focused ion beam scanning electron microscopy (FIB-SEM) images. SEM images were acquired using a JEOL JSM-IT700HR FE-SEM setup in backscattered electron detection mode (acceleration voltage: 5 kV). 3d volumes were created using a dual-beam FIB-SEM (FEI Helios G4 CX). To ensure a smooth sliced surface, a thin (0.5 μm) Pt layer was deposited on the top surface using Pt-GIS installed in the FIB-SEM. An auto slice & view software (ThermoFisher Scientific) was used to automate the alignment, slicing, and acquisition of the high-resolution SEM images. For the FIB-SEM characterization, two different regions of the electrode were scanned to ensure local inhomogeneities could be captured. Volumes of 4.5 μm × 1.8 μm × 1 μm and 4.5 μm × 2.7 μm × 1.7 μm were scanned by slicing different parts of the electrode material, and a slicing distance of 50 nm. Details about the segmentation,[43] microstructure characterization,[46] particle identification algorithms,[40] sub-volume post-processing, and relative statistics can be found in the SI Methods.

### Computational methods

The model's equations were implemented, expanding upon the existing MPET software,[31] and can be found in the SI Methods. The simulations run on a 13$^{th}$ generation Intel Core i9.

# Author contributions

P. O. and A. V. conceived the idea. S. K. P. performed the FIB-SEM characterization. S. K. P. and P. O. segmented the FIB-SEM data and analyzed the microstructures. P. O., S. P., D. N. A. V., and M. B. conceived and developed the model. P. O., D. N., and P. K. designed and performed the electrochemical experiments. P. O. and S. P. implemented the model. A. V., M. W., and

 

M. B. supervised the project. All authors wrote, contributed to, and discussed the final manuscript.

## Conflicts of interest

There are no conflicts to declare.

## Data availability

The dataset is available at https://zenodo.org/records/15683313?token=eyJhbGciOiJIUzUxMiJ9.eyJpZCI6Ijk3NGI0NWVhLTFjY2YtNGUzNy04ZmEwLTc0MTdhMGZiN2YyMSIsImRhdGEiOnt9LCJyYW5kb20iOiI5Y2M4NmY4OTIwYWMyZmM4MThiZTU3NDBjYzgyOGRkZCJ9.oUm5JB3mP01lPRDKH-khUmdsuyaw6GGUKj1ZcDox5a0b5l_OdTn1TXd_KdKSREgqhxBAUUyjwFir2HbidRKBCg.

Additional information on the content of the repository can be found in the supplementary information (SI). Supplementary information: the microstructural data and the relative characterization; the electrochemical data; the results of the simulations. See DOI: https://doi.org/10.1039/d5ee04131g.

The repository also momentarily includes the code necessary to replicate the results.

Code availability: the code needed to replicate the model's results is available online at https://github.com/Ombrini/MPET_Network.

## Acknowledgements

P. O and M. W. acknowledge the support of Shell Global Solutions International B. V.; A. V. acknowledge the Netherlands Organization for Scientific Research (NWO) under the VENI grant nr 18123; S. P. and M. Z. B. acknowledge support from Shell International Exploration & Production, Inc. *via* the MIT Energy Initiative.

## References

1 M. S. Ziegler and J. E. Trancik, Re-examining rates of lithium-ion battery technology improvement and cost decline, *Energy Environ. Sci.*, 2021, **14**, 1635–1651.
2 IEA, *Batteries and Secure Energy Transitions*, IEA, Paris, 2024, https://www.iea.org/reports/batteries-and-secure-energy-transitions.
3 P. Karanth, *et al.*, A phase inversion strategy for low-tortuosity and ultrahigh-mass-loading nickel-rich layered oxide electrodes, *Cell Rep. Phys. Sci.*, 2024, **5**(6), DOI: 10.1016/j.xcrp.2024.101972.
4 E. C. Tredenick, *et al.*, A Multilayer Doyle-Fuller-Newman Model to Optimise the Rate Performance of Bilayer Cathodes in Li Ion Batteries, *J. Electrochem. Soc.*, 2024, **171**, 060531.
5 J. Min, W. Suk, S. C. Y. Wong and Y. Li, Single-Particle Electrochemical Cycling Single-Crystal and Polycrystalline NMC Particles, *Adv. Funct. Mater.*, 2024, **34**(51), DOI: 10.1002/adfm.202410241.
6 S. Lee, L. Su, A. Mesnier, Z. Cui and A. Manthiram, Cracking vs. surface reactivity in high-nickel cathodes for lithium-ion batteries, *Joule*, 2023, **7**, 2430–2444.
7 Y. Samantaray, D. A. Cogswell, A. E. Cohen and M. Z. Bazant, *Electrochemically Resolved Acoustic Emissions from Li-ion Batteries*, *ChemRxiv*, 2025, preprint, DOI: 10.26434/chemrxiv-2025-r7vwq.
8 J. Min, L. M. Gubow, R. J. Hargrave, J. B. Siegel and Y. Li, Direct measurements of size-independent lithium diffusion and reaction times in individual polycrystalline battery particles, *Energy Environ. Sci.*, 2023, **16**, 3847–3859.
9 R. Malik, D. Burch, M. Bazant and G. Ceder, Particle Size Dependence of the Ionic Diffusivity, *Nano Lett.*, 2010, **10**, 4123–4127.
10 D. Fraggedakis, *et al.*, A scaling law to determine phase morphologies during ion intercalation, *Energy Environ. Sci.*, 2020, **13**, 2142–2152.
11 M. Gaberscek, R. Dominko and J. Jamnik, Is small particle size more important than carbon coating? An example study on LiFePO4 cathodes, *Electrochem. Commun.*, 2007, **9**, 2778–2783.
12 E. C. Tredenick, *et al.*, Bridging the Gap between Microstructurally Resolved Computed Tomography-Based and Homogenised Doyle-Fuller-Newman Models for Lithium-Ion Batteries, *J. Electrochem. Soc.*, 2025, **172**, 030503.
13 Y. Li, *et al.*, Effects of Particle Size, Electronic Connectivity, and Incoherent Nanoscale Domains on the Sequence of Lithiation in LiFePO $_4$ Porous Electrodes, *Adv. Mater.*, 2015, **27**, 6591–6597.
14 B. Kang and G. Ceder, Battery materials for ultrafast charging and discharging, *Nature*, 2009, **458**, 190–193.
15 M. M. Doeff, Y. Hu, F. McLarnon and R. Kostecki, Effect of Surface Carbon Structure on the Electrochemical Performance of $LiFePO_4$, *Electrochem. Solid-State Lett.*, 2003, **6**(10), DOI: 10.1149/1.1601372.
16 N. Zhang, *et al.*, Critical Review on Low-Temperature Li-Ion/Metal Batteries, *Adv. Mater.*, 2022, **34**, 2107899.
17 K. A. Seid, *et al.*, Multiscale electronic transport mechanism and true conductivities in amorphous carbon–LiFePO $_4$ nanocomposites, *J. Mater. Chem.*, 2012, **22**, 2641–2649.
18 V. Azimi, A. Allam and S. Onori, Extending Life of Lithium-Ion Battery Systems by Embracing Heterogeneities via an Optimal Control-Based Active Balancing Strategy, *IEEE Trans. Control Syst. Technol.*, 2022, 1–15, DOI: 10.1109/TCST.2022.3215610.
19 W. Li, *et al.*, Online capacity estimation of lithium-ion batteries with deep long short-term memory networks, *J. Power Sources*, 2021, **482**, 228863.
20 L. Xu, J. Cooper, A. Allam and S. Onori, Comparative Analysis of Numerical Methods for Lithium-Ion Battery Electrochemical Modeling, *J. Electrochem. Soc.*, 2023, **170**, 120525.
21 J. W. Haverkort, A theoretical analysis of the optimal electrode thickness and porosity, *Electrochim. Acta*, 2019, **295**, 846–860.
22 M. Doyle, T. F. Fuller and J. Newman, Modeling of Galvanostatic Charge and Discharge of the Lithium/Polymer/Insertion Cell, *J. Electrochem. Soc.*, 1993, **140**, 1526–1533.

23 M. D. Berliner, D. A. Cogswell, M. Z. Bazant and R. D. Braatz, Methods—PETLION: Open-Source Software for Millisecond-Scale Porous Electrode Theory-Based Lithium-Ion Battery Simulations, *J. Electrochem. Soc.*, 2021, **168**, 090504.
24 T. R. Ferguson and M. Z. Bazant, Nonequilibrium Thermodynamics of Porous Electrodes, *J. Electrochem. Soc.*, 2012, **159**, A1967–A1985.
25 K. E. Thomas-Alyea, Modeling Resistive-Reactant and Phase-Change Materials in Battery Electrodes, *ECS Trans.*, 2008, **16**, 155–165.
26 M. Safari and C. Delacourt, Mathematical Modeling of Lithium Iron Phosphate Electrode: Galvanostatic Charge/Discharge and Path Dependence, *J. Electrochem. Soc.*, 2011, **158**, A63.
27 H. D. Deng, *et al.*, Beyond Constant Current: Origin of Pulse-Induced Activation in Phase-Transforming Battery Electrodes, *ACS Nano*, 2024, **18**, 2210–2218.
28 P. Ombrini, M. Z. Bazant, M. Wagemaker and A. Vasileiadis, Thermodynamics of multi-sublattice battery active materials: from an extended regular solution theory to a phase-field model of LiMnyFe1-yPO4, *Npj Comput. Mater.*, 2023, **9**, 148.
29 A. Vasileiadis, *et al.*, Toward Optimal Performance and In-Depth Understanding of Spinel $Li_4Ti_5O_{12}$ Electrodes through Phase Field Modeling, *Adv. Funct. Mater.*, 2018, **28**, 1705992.
30 H. Lian and M. Z. Bazant, Modeling Lithium Plating Onset on Porous Graphite Electrodes Under Fast Charging with Hierarchical Multiphase Porous Electrode Theory, *J. Electrochem. Soc.*, 2024, **171**, 010526.
31 R. B. Smith and M. Z. Bazant, Multiphase Porous Electrode Theory, *J. Electrochem. Soc.*, 2017, **164**, E3291–E3310.
32 H. Zhao, *et al.*, Learning heterogeneous reaction kinetics from X-ray videos pixel by pixel, *Nature*, 2023, **621**, 289–294.
33 T. R. Ferguson and M. Z. Bazant, Phase Transformation Dynamics in Porous Battery Electrodes, *Electrochim. Acta*, 2014, **146**, 89–97.
34 Y. Li, *et al.*, Current-induced transition from particle-by-particle to concurrent intercalation in phase-separating battery electrodes, *Nat. Mater.*, 2014, **13**, 1149–1156.
35 M. Ender, J. Joos, T. Carraro and E. Ivers-Tiffée, Quantitative Characterization of $LiFePO_4$ Cathodes Reconstructed by FIB/SEM Tomography, *J. Electrochem. Soc.*, 2012, **159**, A972–A980.
36 J. Li, *et al.*, Dynamics of particle network in composite battery cathodes, *Science*, 2022, **376**, 517–521.
37 M. Z. Bazant, Unified quantum theory of electrochemical kinetics by coupled ion–electron transfer, *Faraday Discuss.*, 2023, **246**, 60–124.
38 P. Bai, D. A. Cogswell and M. Z. Bazant, Suppression of Phase Separation in $LiFePO_4$ Nanoparticles During Battery Discharge, *Nano Lett.*, 2011, **11**, 4890–4896.
39 H. Rostami, J. Valio, P. Tynjälä, U. Lassi and P. Suominen, Life Cycle of $LiFePO_4$ Batteries: Production, Recycling, and Market Trends, *ChemPhysChem*, 2024, **25**, e202400459.
40 F. L. E. Usseglio-Viretta, *et al.*, MATBOX: An Open-source Microstructure Analysis Toolbox for microstructure generation, segmentation, characterization, visualization, correlation, and meshing, *SoftwareX*, 2022, **17**, 100915.
41 M. Jacomy, T. Venturini, S. Heymann and M. Bastian, ForceAtlas2, a Continuous Graph Layout Algorithm for Handy Network Visualization Designed for the Gephi Software, *PLoS One*, 2014, **9**, e98679.
42 A. A. Hagberg, D. A. Schult and P. J. Swart, *Exploring Network Structure, Dynamics, and Function using NetworkX. in 11–15*, Pasadena, California, 2008, DOI: 10.25080/TCWV9851.
43 S. Berg, *et al.*, Ilastik: interactive machine learning for (bio)image analysis, *Nat. Methods*, 2019, **16**, 1226–1232.
44 J. J. Kuo, S. D. Kang and W. C. Chueh, Contact Resistance of Carbon–$Li_x$(Ni,Mn,Co)$O_2$ Interfaces, *Adv. Energy Mater.*, 2022, **12**, 2201114.
45 V. Becker, O. Birkholz, Y. Gan and M. Kamlah, Modeling the Influence of Particle Shape on Mechanical Compression and Effective Transport Properties in Granular Lithium-Ion Battery Electrodes, *Energy Technol.*, 2021, **9**, 2000886.
46 S. J. Cooper, A. Bertei, P. R. Shearing, J. A. Kilner and N. P. Brandon, TauFactor: An open-source application for calculating tortuosity factors from tomographic data, *SoftwareX*, 2016, **5**, 203–210.
47 D. A. Cogswell and M. Z. Bazant, Theory of Coherent Nucleation in Phase-Separating Nanoparticles, *Nano Lett.*, 2013, **13**, 3036–3041.
48 Y. Zhang, *et al.*, Lithium-ion intercalation by coupled ion-electron transfer, *Science*, 2025, **390**, eadq2541.
49 D. A. Cogswell and M. Z. Bazant, Size-dependent phase morphologies in LiFePO4 battery particles, *Electrochem. Commun.*, 2018, **95**, 33–37.
50 M. Z. Bazant, Thermodynamic stability of driven open systems and control of phase separation by electro-autocatalysis, *Faraday Discuss.*, 2017, **199**, 423–463.
51 W. C. Chueh, *et al.*, Intercalation Pathway in Many-Particle $LiFePO_4$ Electrode Revealed by Nanoscale State-of-Charge Mapping, *Nano Lett.*, 2013, **13**, 866–872.
52 P. Ombrini and Q. Wang, *et al.*, Kinetically induced memory effect in Li-ion batteries, *EES Batteries*, 2025, **1**, 437–449.
53 D. Wycisk, M. Oldenburger, M. G. Stoye, T. Mrkonjic and A. Latz, Modified Plett-model for modeling voltage hysteresis in lithium-ion cells, *J. Energy Storage*, 2022, **52**, 105016.
54 S. Afshar, K. Morris and A. Khajepour, *Fully dynamical representation of a LFP battery cell. 2017 American Control Conference (ACC) 499–504 (IEEE, Seattle, WA, USA, 2017)*, DOI: 10.23919/ACC.2017.7963002.
55 A. Geslin, *et al.*, Dynamic cycling enhances battery lifetime, *Nat. Energy*, 2025, **10**, 172–180.
56 L. O. Valøen and J. N. Reimers, Transport properties of LiPF6-based Li-ion battery electrolytes, *J. Electrochem. Soc.*, 2005, **152**, A882.
57 C. Delacourt, L. Laffont, R. Bouchet and C. Wurm, Toward Understanding of Electrical Limitations (Electronic, Ionic) in LiMPO4 (M = Fe, Mn) Electrode Materials, *J. Electrochem. Soc.*, 2005, **152**(5), DOI: 10.1149/1.1884787.
58 X. Wu, *et al.*, Carbon-Nanotube-Decorated Nano-$LiFePO_4$@C Cathode Material with Superior High-Rate and Low-

 

Temperature Performances for Lithium-Ion Batteries, *Adv. Energy Mater.*, 2013, **3**, 1155–1160.
59 S. Kench, *et al.*, Li-ion battery design through microstructural optimization using generative AI, *Matter*, 2024, **7**(12), 4260–4269.
60 Y. Oh, *et al.*, Enhanced Electrical Connectivity in High Energy Density Single-Crystal NCA Electrodes via Polycrystalline Blending Design, *ACS Appl. Mater. Interfaces*, 2025, **17**, 28094–28102.
61 M. He, *et al.*, High power NVPF/HC-based sodium-ion batteries, *J. Power Sources*, 2023, **588**, 233741.